Title

Temperature-Dependent Detectivity of Near-Infrared Organic Bulk Heterojunction Photodiodes

Journal

ACS Applied Materials & Interfaces, 9(2)

ISSN

1944-8244

Authors

Wu, Zhenghui
Yao, Weichuan
London, Alexander E
et al.

Publication Date

2017-01-18

DOI

10.1021/acsami.6b12162

Peer reviewed

ACS APPLIED MATERIALS & INTERFACES

Research Article

www.acsami.org

Temperature-Dependent Detectivity of Near-Infrared Organic Bulk Heterojunction Photodiodes

Zhenghui Wu,[†] Weichuan Yao,[†] Alexander E. London,[‡] Jason D. Azoulay,[‡] and Tse Nga Ng*[,†]

[†]Department of Electrical and Computer Engineering, University of California San Diego, 9500 Gilman Drive, La Jolla, California 92093, United States

[‡]School of Polymers and High Performance Materials, University of Southern Mississippi, 118 College Drive #5050, Hattiesburg, Mississippi 39406, United States

ABSTRACT: Bulk heterojunction photodiodes are fabricated using a new donor−acceptor polymer with a near-infrared absorption edge at 1.2 μm, achieving a detectivity up to 10^{12} Jones at a wavelength of 1 μm and an excellent linear dynamic range of 86 dB. The photodiode detectivity is maximized by operating at zero bias to suppress dark current, while a thin 175 nm active layer is used to facilitate charge collection without reverse bias. Analysis of the temperature dependence of the dark current and spectral response demonstrates a 2.8-fold increase in detectivity as the temperature was lowered from 44 to −12 °C, a relatively small change when compared to that of inorganic-based devices. The near-infrared photodiode shows a switching speed reaching up to 120 μs without an external bias. An application using our NIR photodiode to detect arterial pulses of a fingertip is demonstrated.

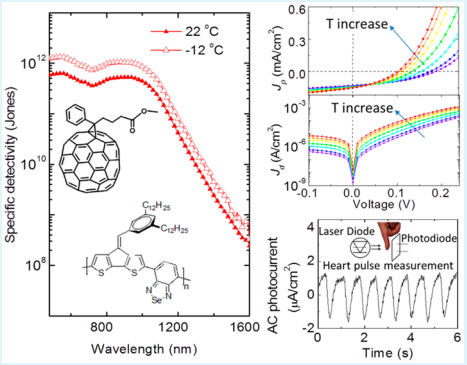

KEYWORDS: *near-infrared photodetector, organic bulk heterojunction, detectivity, temperature dependence, physiological sensing, activation energy*

1. INTRODUCTION

Near-infrared (NIR) photodetectors are needed for a wide variety of applications[1−3] including surveillance, environmental monitoring, optical communications, and spectroscopic instrumentation. For a broad, tunable response in the NIR spectral region (0.8−1.4 μm), narrow bandgap conjugated copolymers[4−6] are a promising alternative to conventional III−V inorganic semiconductors, which require high-temperature growth and are limited by die transfer and bonding processes. In contrast, organic semiconductors allow direct deposition and low temperature processing (<200 °C) simplifying fabrication and potentially enabling high spatial resolution in focal plane arrays.

The bulk heterojunction (BHJ) architecture has been key to making efficient organic photovoltaics[6−9] and the same attributes make it ideal for photodetectors.[10−13] In the NIR, state-of-the-art BHJ photodiodes[13,14] show a relatively low external quantum efficiency (EQE) up to 6.5%; however, due to very low dark current, the organic photodiodes (OPDs) reach a detectivity of 10^{12} Jones at room temperature, superior to that of their uncooled inorganic counterparts. Previous work by Zimmerman et al.[14] employed a molecular porphyrin-tape dimer with absorption peaks between the wavelengths of λ = 1050 and 1350 nm to fabricate NIR OPDs, but the crystallinity of the material led to a relatively rough film morphology that restricted the processing tolerance window. A hybrid organic BHJ photodiode with PbS quantum dot sensitizers[3] achieved detection up to 1.8 μm; however, the photodiode rectification ratio was only ∼6000 and did not allow high detectivity due to the rough topology from the quantum dot particles. Instead of crystalline materials, Gong et al.[15] used an amorphous conjugated polymer with absorption maxima (λ_{max}) at 850 nm and a long absorption tail extending to 1400 nm. While many strategies exist to modify the properties of conjugated materials, molecular species with absorption profiles above 1 μm remain difficult to access and generally exhibit low optical sensitivity.

Here, we demonstrate a NIR photodiode employing a new conjugated polymer with λ_{max} = 920 nm and an absorption edge at 1200 nm. The molecular structure is shown in Figure 1, and full details regarding the synthesis will be published elsewhere. Due to the weak optical response at the tail of the absorption spectrum, the BHJ film thickness is often increased to enhance light absorption, while a reverse bias is applied to boost charge collection.[12,16,17] This study investigates the effect of film thickness and the approach to maximize detectivity through the use of thinner films without the need of an external bias. Furthermore, we obtain the photocurrent and dark current characteristics in a temperature range of 44 to −12 °C, typical for indoor applications, to examine the carrier transport and recombination processes.[18,19] We also proceed to compare the activation energy of both photocurrent and dark current.

Received: September 24, 2016
Accepted: December 17, 2016
Published: December 17, 2016

DOI: 10.1021/acsami.6b12162
ACS Appl. Mater. Interfaces XXXX, XXX, XXX−XXX

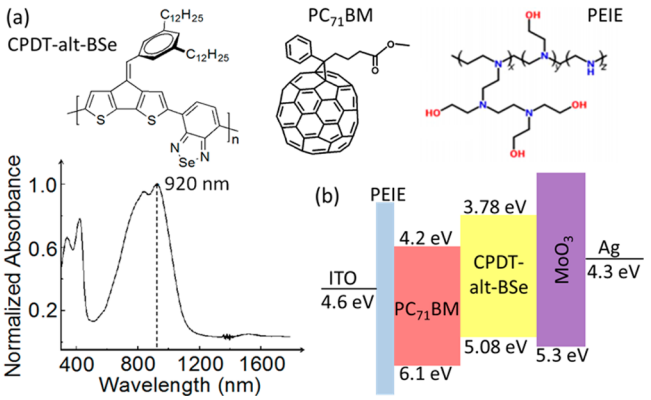

Figure 1. (a) Chemical structures of the organic materials used in the fabrication of the NIR photodiode and the absorption spectrum of the copolymer measured on a thin film. (b) Energy diagram of the photodiode.

Previous work reported rising EQE with higher temperature in organic photodiodes due to thermally activated transport in the BHJ.[20] While we observe this same trend, we present a comprehensive temperature-dependent signal-to-noise analysis and show how detectivity improves with decreasing temperature in NIR BHJ photodiodes. Lastly, we characterize the switching speed and demonstrate an application example using our NIR photodiode to detect arterial pulses of a fingertip.

2. RESULTS AND DISCUSSION

2.1. Materials and Device Structure. The device structure of the NIR photodiode is shown in Figure 1 along with the energy diagram of the materials. The low work function of 80% ethoxylated polyethylenimine (PEIE)-modified indium tin oxide (ITO) favors the collection of electrons at the cathode.[21] MoO_3 is used as the electron-blocking layer at the anode and matches the highest occupied molecular orbital (HOMO) level of the polymer.[22] The near-infrared absorbing material used in the fabrication of the BHJ photodiode is a polymer comprised of an exocyclic olefin subsituted 4*H*-cyclopenta[2,1-*b*:3,4-*b*′]dithiophene (CPDT) donor and a 2,1,3-benzoselenadiazole acceptor (CPDT-*alt*-BSe) (with a number-average molecular weight M_n = 10 kg mol^{-1} and dispersity (Đ = 2.9). Closely related alternating donor/acceptor units along the backbones of conjugated copolymers have proven beneficial for achieving promising optoelectronic functionality.[4,5,23] This particular combination yields a reduction in the band gap when compared to other substitution patterns. The details of the synthesis will be published elsewhere. The unique and advantageous properties of this polymer include: (1) solubility as high as 25 mg/mL, which benefits solution-processed large-scale production; (2) sharp absorption edge, which indicates low density of trap states and ensures that the photoresponse within 1150 nm is due to gap-to-gap excition that facilitates fast temporal response. Fullerene derivative [6,6]-phenyl-C71-butyric acid methyl ester ($PC_{71}BM$) (Ossila Ltd.) and the cathode interfacial layer PEIE (35−40 wt % in water, molecular weight 7000 g/mol, Sigma-Aldrich) were used as purchased without further purification.

2.2. Photoresponse and Dark Current. Figure 2 shows devices with linear photoresponse up to the illumination power $P_{illumin}$ of 1 mW/cm^2. Here we fabricated photodiodes with two different BHJ layer thicknesses. The photocurrent of the thin

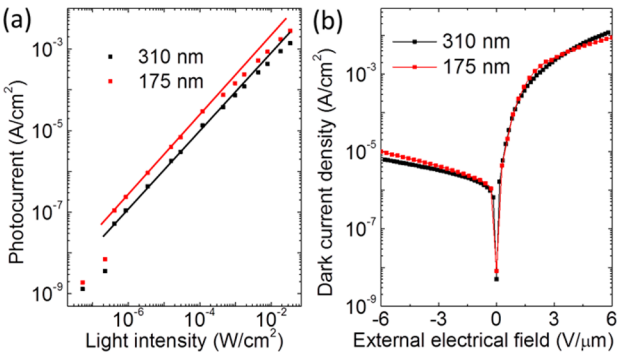

Figure 2. Comparison of two photodiodes with different BHJ thicknesses. (a) Photocurrent density as a function of light intensity at wavelength of 904 nm and at zero external bias. (b) Dark current density as a function of the applied electric field.

175 nm device is higher than that of the thick 310 nm device, but the dark current is worse for the thin photodiode than for the thick one, indicating a trade-off between the dark current and photocurrent as the BHJ thickness is varied.[24,25] The linear dynamic range (LDR) is calculated from LDR= 20 log($J_{max,linear}/J_{min,linear}$), where $J_{max,linear}$ and $J_{min,linear}$ are the maximum and minimum photocurrent densities within the linear photoresponse region (within 0.5 μW/cm^2 to 5 mW/cm^2), respectively. The thick (310 nm) device shows LDR of 63 dB, and the thin (175 nm) device shows LDR of 86 dB, which is comparable to that of the typical InGaAs photodetectors as provided in vendor specifications,[26] where the dynamic range is reported to be 13 000 to 16 666, equivalent to 82−84 dB according to the above LDR calculation.

The figure of merit for a photodetector is the detectivity,[27] a signal-to-noise ratio defined as $D^* = (A\Delta f)^{1/2} R/i_n$, where $R = J_{photo}/P_{illumin}$ is the responsivity in ampere/watt, A is the effective photodetector area in cm^2, Δf is the electrical bandwidth in Hertz, and i_n is the noise current measured in the dark. The detectivity unit is Hz$^{1/2}$ cm W^{-1} or Jones. As shown in Figure 2a, the lowest photocurrent detected by lock-in amplifier at weak illumination for the two devices are around 2 nA/cm^2. This value is already lower than that of the $I-V$ measurements. Therefore, it is reasonable to apply the assumption that the detector noise is limited by the dark current density,[15] and we calculate the detectivity from $D^* = R/(2qJ_d)^{1/2}$, where J_d is the dark current density from $I-V$ characteristics and q is the electron charge. The photodiodes need high photoresponse and low dark current density to reach high detectivity. In the following section, we examine the photocurrent and dark current characteristics under varying temperature to gain insights into the carrier transport and recombination limitations in the NIR BHJ photodiodes.

2.3. Photoresponse and Dark Current at Different Operational Temperatures. The temperature-dependent characteristics for the two devices under 8 mW/cm^2 white light illumination are shown in Figure 3a. The temperature-dependent measurements were conducted in the typical working temperature range of wearable electronics (−12 to 44 °C) for the goal of physiological monitoring application. With rising temperature, the current density increases, and the open-circuit voltage decreases. The empirical Arrhenius equation is used to quantify the temperature dependence of the photocurrent density $J_{photo}(T) = J_{0,photo} \exp(-\Delta_{photo}/kT)$, where $J_{0,photo}$ is a prefactor influenced by photogenerated carriers, electrical field, and mobility; Δ_{photo} is the activation

DOI: 10.1021/acsami.6b12162
ACS Appl. Mater. Interfaces XXXX, XXX, XXX−XXX

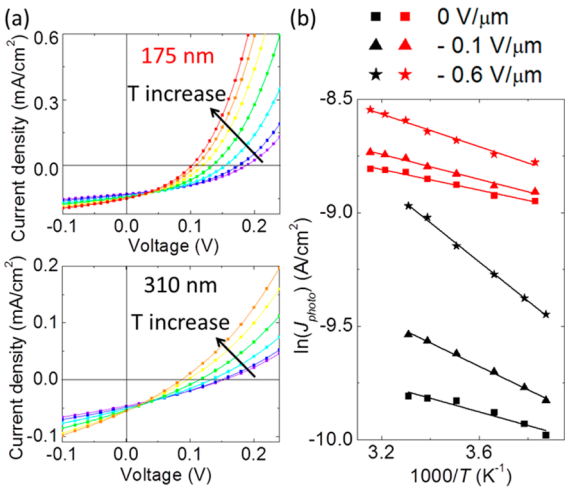

Figure 3. (a) $J-V$ characteristics at different temperature T under 8 mW/cm^2 white light illumination. For the device with 175 nm BHJ film, the measurements were taken at T = −12, 0, 12, 22, 30, 38, and 44 °C. For the device with 310 nm BHJ film, the measurements were taken at T = −15, −9, 0, 12, 22, and 30 °C. (b) Natural logarithm of photocurrent densities versus temperature under different applied electric fields. Red data points are for the device with 175 nm BHJ film, black for 310 nm film.

energy[28] indicating the trap depth or the degree of disorder in the photodiode under illumination; k is the Boltzmann constant; and T is the temperature. Assuming that charge generation and dissociation processes are not significantly affected in the temperature range chosen for this study, the activation energy is interpreted as the average trap depth that determines the probability for re-emission of trapped carriers. The parameter values in Table 1 are obtained by linear regression as shown in Figure 3b. To compare the devices properly under the same electric field, the applied reverse bias is adjusted for BHJ thicknesses; for example, we use a reverse bias at −0.18 V for the 310 nm device and one of −0.1 V for the 175 nm device so that the applied electrical fields are equivalent.

Table 1. Parameters Obtained from Measurements of Photocurrent Density versus Temperature under 8 mW/cm^2 White Light Illumination

BHJ thickness (nm)	applied electric field (V/um)	Δ_{photo} (meV)	$J_{0,photo}$ (mA/cm^2)
310	0	26 ± 3	0.15 ± 0.02
	−0.1	45 ± 2	0.40 ± 0.02
	−0.6	75 ± 2	2.20 ± 0.11
175	0	20 ± 1	0.31 ± 0.01
	−0.1	24 ± 1	0.39 ± 0.02
	−0.6	31 ± 2	0.60 ± 0.03

The photocurrent prefactor $J_{0,photo}$ increases under reverse bias. Δ_{photo} is higher for the 310 nm film than for the 175 nm one, which indicates that the trap depth is deeper, and it requires more energy. Hence, it is more difficult to delocalize the carriers stuck in trap sites in the thick device than in the thin one. This finding implies worsening charge collection efficiency and explains the reduced photocurrent in the thick device. The overall photocurrent is lower at zero bias than under reverse bias, but it is worth noting that Δ_{photo} is smaller at zero bias than under reverse bias. It seems counterintuitive that charge detrapping may occur at low energy levels at zero bias. The likely explanation is that at zero bias the only available carriers are charge from shallow trap states whereas under reverse bias carriers from deeper traps become accessible and measurable in the photocurrent. The electric-field-assisted barrier lowering[29] results in carriers being released from the traps and contributes to the increase of Δ_{photo} under reverse bias. In our particular system, the reduced Δ_{photo} at zero bias indicates a potential path to minimize temperature effects on photocurrent through operating photodiodes at zero bias.

Figure 4 shows the temperature-dependent characteristics measured in the dark. The dark current increases by an order of magnitude upon applying reverse bias. The sharp increase in dark current under an applied bias is due to Poole−Frenkel electric-field-assisted emission[30] of charge from trapped sites. Moreover, injection current[31] from one or both of the electrodes may contribute to the dark current. While we have already employed electrode interfacial layers to reduce recombination at the electrodes, further optimization of the charge blocking layers[32] may reduce the dark current.

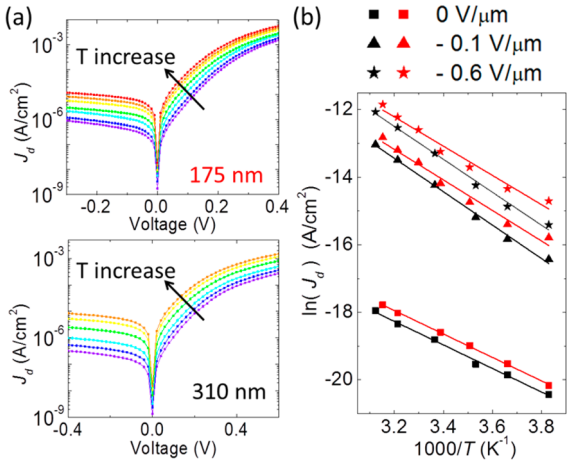

Figure 4. (a) $J-V$ characteristics in the dark at different temperature T. For the device with 175 nm BHJ film, the measurements were taken at T = −12, 0, 12, 22, 30, 38, and 44 °C. For the device with 310 nm BHJ film, the measurements were taken a T = −12, 0, 10, 24, 38, and 47 °C. (b) Natural logarithm of dark current densities versus temperature under different applied electric fields. Red data points are for the device with 175 nm BHJ film, black points are for the device with 310 nm film.

The empirical expression $J_d(T) = J_{0,d} \exp(-\Delta_d/kT)$ is used to quantify the temperature effect on the current density in the dark. Here activation energy Δ_d is influenced by thermal generation and electric-field-assisted emission. The linear regression values are summarized in Table 2. The dark current

Table 2. Parameters Obtained from Measurements of Dark Current Density versus Temperature

BHJ thickness (nm)	applied electric field (V/μm)	Δ_d (meV)	$J_{0,d}$ (mA/cm^2)
310	0	303 ± 10	0.9 ± 0.3
	−0.1	430 ± 14	1.3 ± 0.7
	−0.6	424 ± 18	2.9 ± 1.7
175	0	302 ± 4	1.1 ± 0.2
	−0.1	393 ± 25	5.7 ± 4.4
	−0.6	377 ± 27	8.6 ± 6.8

DOI: 10.1021/acsami.6b12162
ACS Appl. Mater. Interfaces XXXX, XXX, XXX−XXX

prefactor $J_{0,d}$ increases with applied bias. The thin photodiode shows slightly higher $J_{0,d}$ and worse noise spectral density compared to those of the thick device. The data in Tables 1 and 2 lead to the following three observations on the activation-energy parameter: (1) The Δ_d's are the same within one standard deviation for both devices; hence, changing BHJ thickness has negligible effect on the activation energy. (2) Δ_d is higher under reverse bias than at zero bias. (3) Δ_d values measured in the dark are at least 6× higher than Δ_{photo} obtained under illumination.

The first observation, that Δ_d is not affected by the BHJ thickness, is in agreement with the BHJ model,[6,32,33] where thermalization of carriers is mainly influenced by the energy level of charge-transfer states. The second observation is a result of the electric-field-assisted emission[30] that allows carriers being released from the deep traps. The third observation underscores that the dark current is more sensitive to temperature than photocurrent. In the absence of an applied field, the main contributions to dark current are from the two temperature-dependent processes: (a) generation of intrinsic carriers by thermal excitation from valence band to conduction band and (b) generation−recombination (G-R) of intrinsic carriers due to traps and defects. In contrast, the main contributing factor to photocurrent is the photogeneration of free carriers, and temperature has negligible effect on photogeneration. Under illumination, temperature only affects the carrier loss due to trap-assisted recombination in charge transport and collection. Hence, the photocurrent density is less sensitive to temperature changes than dark current density.

In terms of the noise spectral density, increasing the BHJ thickness leads to counteracting effects on the dark current density, in which on the one hand there is increased series resistance lowering the dark current but on the other hand there are additional G-R events adding to the dark current. Therefore, increasing the BHJ thickness is only moderately effective in suppressing the dark current in our system. In terms of photocurrent density, more photogenerated carriers are lost in the thick device than in the thin one because of deeper traps as evident from comparing Δ_{photo}. Similar to the thickness dependence in organic photovoltaics, here the thin 175 nm device shows detectivity D^* better than that of the thick 310 nm device (Figure 5).

2.4. Analysis of External Quantum Efficiency and Detectivity. The external quantum efficiency (EQE) is defined as the ratio of the number of charge collected (n_e) to the number of incident photons (n_{ph}): $EQE(\lambda) = n_e/n_{ph} = (J_{photo}/q)(hc/\lambda P_{illumin}) = R(hc/\lambda q)$, where J_{photo} is the photocurrent density, c is the speed of light, h is Planck's constant, $P_{illumin}$ is the intensity of the incident light, and λ is the wavelength of the incident light. EQE and D^* are related by the responsivity $R(\lambda) = J_{photo}/P_{illumin}$. In Figure 5, for the range of 480−700 nm, the additional photoresponse of PCBM makes the EQE spectrum different from the absorption spectrum of the polymer alone as shown in Figure 1. In the range of 700−1200 nm, the shape of the EQE spectrum differs from the absorption spectrum of the pristine polymer due to two reasons: (1) The blend film includes charge-transfer states arising from interaction between the polymer and PCBM; (2) Additional factors besides absorption that affect EQE. Based on the working mechanism of photodiode, EQE can be expressed as $EQE(\lambda) = \eta_{abs}(\lambda)\cdot\eta_{diss}(\lambda)\cdot\eta_{coll}(\lambda)$, where η_{abs} is the light absorption efficiency in the blend layer, η_{diss} is the dissociation efficiency of the excitons generated in the bulk or at the D−A interface

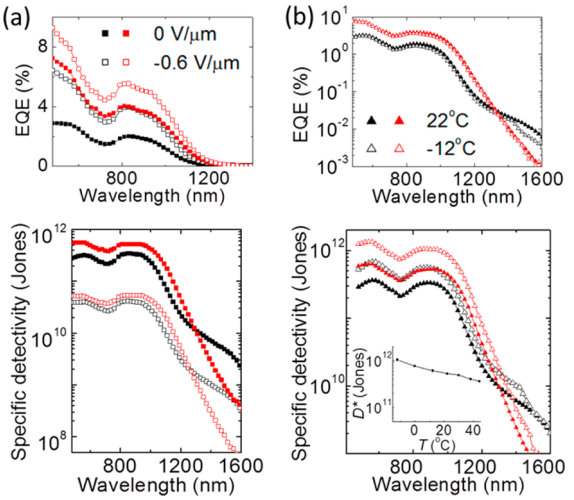

Figure 5. Spectral dependence of the external quantum efficiency and the detectivity under different (a) applied electric field and (b) operating temperature at zero bias. The black curves are measured on the device with a 310 nm BHJ layer, and the red curves are on the device with a 175 nm BHJ layer. The inset plot shows the detectivity at λ = 900 nm of the 175 nm OPD at T = −12, 0, 12, 22, 30, 38, and 44 °C.

due to charge transfer (CT) states, and η_{coll} characterize the efficiency of charge transport through the device. As shown previously,[10] the carriers generated at different wavelengths show different spatial distributions due to different absorption coefficients and interference effects, which in turn affect η_{coll}. $\eta_{diss}(\lambda)$ and $\eta_{coll}(\lambda)$ contribute to EQE; hence, the shape of EQE spectrum for organic photodiode is usually not the same as the absorption spectrum.

The spectral responses for the two photodiodes in Figure 5 show an interesting transition in EQE and D^* near the absorption edge at 1.2 μm. From the visible region to the near-infrared region up to 1.2 μm, absorption corresponds to the polymer or the fullerene bandgaps, and the thin device has superior performance to that of the thick device. However, the thin device response is overtaken by that of the thick device in the region beyond 1.2 μm, where the absorption due to CT states dominates.[34,35] The thickness effect has been used to tune the photodetector spectral window,[10] but the previous work is not aimed at the CT states as shown here. As the thickness of the organic blend layer increases, the area of donor−acceptor interfaces increases correspondingly. Larger interface area means stronger absorption by CT states, which is the reason that the thick photodiode performs better than does the thin device at spectral region from 1200 to 1600 nm.

Figure 5 presents the photodiode spectral response at different applied electric field and operational temperature. The EQE improves by only 2% upon applying an electric field of −0.6 V/μm. For the photodiodes in this study, the best detectivity is achieved at zero bias because a small reverse bias increases the dark current by 10 times but the photocurrent does not increase as much. The detectivity of the photodiodes operated at 22 and −12 °C is compared in Figure 5b, and the effect of temperature is uniform across the spectral range except near the absorption edge. Due to thermally activated hopping transport in organic semiconductors, the photocurrent is lowered as temperature decreases; nevertheless, as mentioned in our earlier discussions on activation energies, the photocurrent decreases less than dark current does when operating

DOI: 10.1021/acsami.6b12162
ACS Appl. Mater. Interfaces XXXX, XXX, XXX−XXX

temperature is reduced. As a result, the detectivity still improves with decreasing temperature. For instance, the detectivity at λ = 900 nm of the 175 nm OPD increases by about 2.8 times as temperature is lowered from 44 to −12 °C, with D^*(44 °C) = 3.65 × 10^{11} Jones and D^*(−12 °C) = 1.04 × 10^{12} Jones, respectively. For the same temperature range, the detectivity of inorganic photodetectors changes by an order of magnitude.[36] In contrast, the temperature dependence of OPDs is relatively small, indicating that organic photodiodes are suitable for ambient operation, offering the option to bypass active temperature control to cool the detector.

2.5. Temporal Response. Figure 6a shows the temporal response of the photodiode with a 175 nm BHJ film, in which

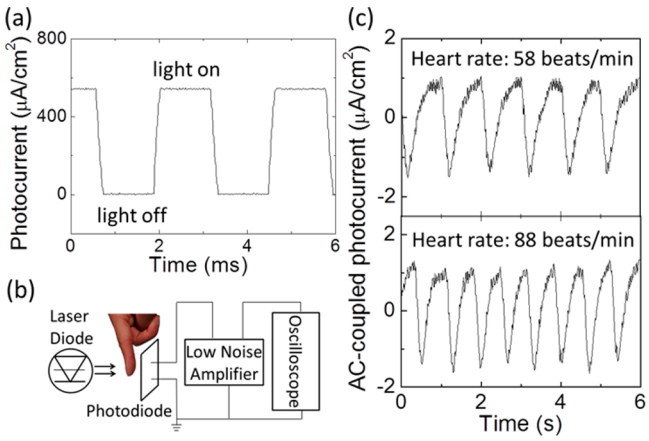

Figure 6. (a) Temporal response of a photodiode illuminated by a NIR 904 nm laser diode. The light power is 30 mW/cm^2, and the light beam is modulated with a mechanical chopper rotating at 390 Hz. (b) Schematic diagram of the heart rate measurement. A 904 nm, 1 mW laser shone NIR light through the finger, and the transmitted light was measured by the organic photodiode showing signal modulation due to arterial pulses. The oscilloscope is in ac-coupled mode. (c) Photocurrent signals tracking a person's heart rate.

the rise and fall times are 110 and 120 μs, respectively, under illumination of 30 mW/cm^2 and connected to a load resistor of 100 Ω. The switching time slows down to 320 μs when illumination power is lowered to 30 μW/cm^2. The switching time measured at lower illumination power is longer for two reasons: (1) There was less carrier density generated and lower diffusion potential. (2) When the illumination power is low, a larger load resistor was used to increase gain (100 kΩ for high gain, 100 Ω for low gain). The load resistor is only a fraction of the total resistance since the photodiode resistance is in the MΩ range; however, the high-gain resistance is significant enough to increase the RC time. If the load resistor is unchanged and light intensity increases from 1 to 40 μW/cm^2, then the rise/fall time will shorten by about 10%. The temporal response shown here is more than sufficient for tracking physiological signals such as heart rate and blood oxygenation. While previous demonstrations[37,38] with flexible organic photodiodes focus on the visible wavelength region, here we utilize NIR detection, which has deeper penetration depth in biological tissues.

Figure 6b is a schematic for using our NIR photodiode to monitor heart beats through detecting light transmission change at a fingertip. A volunteer signed a consent form for the measurements of heart rate. Near-infrared light from a laser diode (wavelength of λ = 904 nm and power at 1 mW/cm^2) is used as the light source, and a finger is placed between the light source and the photodiode. As a person's heart pumps blood into the fingertip, the transmitted light is modulated according to the changing blood volume. The light modulation is measured by our photodiode, and the temporal signal allows inference of the heart pulse rate. Figure 6c shows the photodiode measurement of the heart rate for a person at rest and after exercise.

3. CONCLUSIONS

In summary, the NIR photodiodes using a novel narrow bandgap conjugated polymer demonstrated high detectivity up to 10^{12} Jones at −12 °C and linearity dynamic range of 86 dB. Here the detectivity was maximized by operating at zero bias to suppress dark current; similar to organic photovoltaics, a thin 175 nm BHJ layer was used to facilitate charge collection without reverse bias. Though the organic photodiode detectivity tripled by cooling from 44 to −12 °C, the temperature dependence of OPDs is relatively small compared to that of inorganic NIR detectors. As an application example, we successfully tracked a person's heart rate by placing the organic photodiode directly on a finger. A 904 nm, 1 mW laser shone NIR light through the finger, and the transmitted light was measured by the organic photodiode showing signal modulation due to arterial pulses. The switching rate of the organic photodiode reaches up to 120 μs and is promising for future integration into a real-time NIR imaging system.

4. EXPERIMENTAL SECTION

The prepatterned ITO substrate was ultrasonically cleaned in detergent and deionized water and 2-propanol for 15 min sequentially. PEIE was diluted by 2-methoxyethanol to achieve a concentration of 0.4% by weight. The diluted PEIE solution was cast onto the cleaned ITO substrate at a spin speed of 3500 rpm to form a ∼ 10 nm film, which was annealed at 120 °C for 10 min in ambient. The polymer and $PC_{71}BM$ in a 1:2 ratio were dissolved into a mixed solvent of 3:1 chlorobenzene/chloroform. The solutions were stirred on a hot plate at 45 °C overnight in N_2 atmosphere. Then, the solution with a concentration of 14 or 22 mg/mL for polymer was spin-coated on the PEIE/ITO substrate with spin speed of 1800 rpm to form films with a thickness of 175 or 310 nm, respectively. To complete the fabrication of the OPD, 15 nm MoO_3, followed by 100 nm Ag, was deposited on top of the blend film through thermal evaporation in a vacuum chamber with a pressure of 3 × 10^{-6} mbar. The effective areas of these photodetectors were 8.5 mm^2, which were measured with the help of an optical microscope. The devices were encapsulated between glass slides bonded with epoxy. Subsequently, the devices were characterized in air on a Peltier stage during variable temperature measurement. The photodiode spectral response was amplified through a low-noise amplifier with an internal load resistor of 100 kΩ (for high gain) or 100 Ω (for low gain) and measured with a lock-in amplifier, using a monochromatic light source modulated by a mechanical chopper at a frequency of 390 Hz. Cutoff filters at 455, 645, and 1025 nm were used to reduce the scattered light due to higher order diffraction. The lock-in amplifier can accurately measure a modulated photocurrent down to a magnitude of 2 × 10^{-11} A. For the temporal response measurement, the photodiode signal was amplified through a low-noise amplifier at gain of 20 μA/V before being connected to an oscilloscope.

AUTHOR INFORMATION

Corresponding Author

*E-mail: tnn046@ucsd.edu.

ORCID

Zhenghui Wu: 0000-0002-4187-9280

DOI: 10.1021/acsami.6b12162
ACS Appl. Mater. Interfaces XXXX, XXX, XXX−XXX

Author Contributions

T.N.N. and Z.W. designed the experiment. J.D.A. designed the polymer synthesis while A.E.L. carried out the synthesis. Z.W. and W.Y. fabricated the photodiodes and performed device characterization.

Funding

UCSD ECE start-up funds; National Science Foundation (DGE-1449999), (CMMI-1635729).

Notes

The authors declare no competing financial interest.

■ ACKNOWLEDGMENTS

We gratefully thank Prof. Bryan Wong at UC Riverside for predictive calculations. Z.W., W.Y., and T.N.N. thank the financial support from UCSD ECE start-up funds. Z.W., W.Y., and T.N.N. acknowledge support from the National Science Foundation (CMMI-1635729). A.E.L. and J.D.A. wish to acknowledge financial support from the National Science Foundation (DGE-1449999).

■ REFERENCES

(1) Rogalski, A. Recent Progress in Infrared Detector Technologies. *Infrared Phys. Technol.* **2011**, *54* (3), 136−154.
(2) Konstantatos, G.; Sargent, E. H. Nanostructured Materials for Photon Detection. *Nat. Nanotechnol.* **2010**, *5* (6), 391−400.
(3) Rauch, T.; Boberl, M.; Tedde, S. F.; Furst, J.; Kovalenko, M.; Hesser, G.; Lemmer, U.; Heiss, W.; Hayden, O. Near-Infrared Imaging with Quantum-Dot-Sensitized Organic Photodiodes. *Nat. Photonics* **2009**, *3*, 332−336.
(4) Foster, M. E.; Zhang, B. a; Murtagh, D.; Liu, Y.; Sfeir, M. Y.; Wong, B. M.; Azoulay, J. D. Solution-Processable Donor-Acceptor Polymers with Modular Electronic Properties and Very Narrow Bandgaps. *Macromol. Rapid Commun.* **2014**, *35* (17), 1516−1521.
(5) Azoulay, J. D.; Koretz, Z. A.; Wong, B. M.; Bazan, G. C. Bridgehead Imine Substituted Cyclopentadithiophene Derivatives: An Effective Strategy for Band Gap Control in Donor − Acceptor Polymers. *Macromolecules* **2013**, *46*, 1337−1342.
(6) Dou, L.; You, J.; Hong, Z.; Xu, Z.; Li, G.; Street, R. A.; Yang, Y. 25Th Anniversary Article: A Decade of Organic/Polymeric Photovoltaic Research. *Adv. Mater.* **2013**, *25* (46), 6642−6671.
(7) Dennler, G.; Scharber, M. C.; Brabec, C. J. Polymer-Fullerene Bulk-Heterojunction Solar Cells. *Adv. Mater.* **2009**, *21* (13), 1323−1338.
(8) Yip, H.-L.; Jen, A. K.-Y. Recent Advances in Solution-Processed Interfacial Materials for Efficient and Stable Polymer Solar Cells. *Energy Environ. Sci.* **2012**, *5* (3), 5994.
(9) Scharber, M. C.; Sariciftci, N. S. Efficiency of Bulk-Heterojunction Organic Solar Cells. *Prog. Polym. Sci.* **2013**, *38* (12), 1929−1940.
(10) Armin, A.; Jansen-van Vuuren, R. D.; Kopidakis, N.; Burn, P. L.; Meredith, P. Narrowband Light Detection via Internal Quantum Efficiency Manipulation of Organic Photodiodes. *Nat. Commun.* **2015**, *6*, 6343.
(11) Ng, T. N.; Wong, W. S.; Lujan, R. A.; Street, R. A. Characterization of Charge Collection in Photodiodes under Mechanical Strain: Comparison between Organic Bulk Heterojunction and Amorphous Silicon. *Adv. Mater.* **2009**, *21* (18), 1855−1859.
(12) Ng, T. N.; Wong, W. S.; Chabinyc, M. L.; Sambandan, S.; Street, R. A. Flexible Image Sensor Array with Bulk Heterojunction Organic Photodiode. *Appl. Phys. Lett.* **2008**, *92* (21), 213303.
(13) Street, R. A.; Ng, T. N.; Schwartz, D. E.; Whiting, G. L.; Lu, J. P.; Bringans, R. D.; Veres, J. From printed transistors to printed smart systems. *Proc. IEEE* **2015**, *103* (4), 607−618.
(14) Zimmerman, J. D.; Diev, V. V.; Hanson, K.; Lunt, R. R.; Yu, E. K.; Thompson, M. E.; Forrest, S. R. Porphyrin-tape/C(60) Organic Photodetectors with 6.5% External Quantum Efficiency in the near Infrared. *Adv. Mater.* **2010**, *22* (25), 2780−2783.
(15) Gong, X.; Tong, M.; Xia, Y.; Cai, W.; Moon, J. S.; Cao, Y.; Yu, G.; Shieh, C.-L.; Nilsson, B.; Heeger, A. J. High-Detectivity Polymer Photodetectors with Spectral Response from 300 Nm to 1450 Nm. *Science* **2009**, *325* (5948), 1665−1667.
(16) Yang, C. M.; Tsai, P. Y.; Horng, S. F.; Lee, K. C.; Tzeng, S. R.; Meng, H. F.; Shy, J. T.; Shu, C. F. Infrared Photocurrent Response of Charge-Transfer Exciton in Polymer Bulk Heterojunction. *Appl. Phys. Lett.* **2008**, *92* (8), 083504.
(17) Chan, K. K. H.; Tsang, S. W.; Lee, H. K. H.; So, F.; So, S. K. Charge Transport Study of Semiconducting Polymers and Their Bulk Heterojunction Blends by Capacitance Measurements. *J. Polym. Sci., Part B: Polym. Phys.* **2013**, *51* (8), 649−658.
(18) Chirvase, D.; Chiguvare, Z.; Knipper, M.; Parisi, J.; Dyakonov, V.; Hummelen, J. C. Temperature Dependent Characteristics of poly(3 Hexylthiophene)-Fullerene Based Heterojunction Organic Solar Cells. *J. Appl. Phys.* **2003**, *93* (6), 3376−3383.
(19) Thakur, A. K.; Wantz, G.; Garcia-Belmonte, G.; Bisquert, J.; Hirsch, L. Temperature Dependence of Open-Circuit Voltage and Recombination Processes in Polymer-Fullerene Based Solar Cells. *Sol. Energy Mater. Sol. Cells* **2011**, *95* (8), 2131−2135.
(20) Schilinsky, P.; Waldauf, C.; Brabec, C. J. Recombination and Loss Analysis in Polythiophene Based Bulk Heterojunction Photodetectors. *Appl. Phys. Lett.* **2002**, *81* (20), 3885−3887.
(21) Zhou, Y.; Fuentes-hernandez, C.; Shim, J.; Meyer, J.; Giordano, A. J.; Li, H.; Winget, P.; Papadopoulos, T.; Cheun, H.; Kim, J.; Fenoll, M.; Dindar, A.; Haske, W.; Najafabadi, E.; Khan, T. M.; Sojoudi, H.; Barlow, S.; Graham, S.; Brédas, J.; Marder, S. R.; Kahn, A.; Kippelen, B. A Universial Method to Produce Low-Work Function Electrodes for Organic Electronics. *Science* **2012**, *336*, 327−332.
(22) Ajuria, J.; Etxebarria, I.; Cambarau, W.; Muñecas, U.; Tena-Zaera, R.; Jimeno, J. C.; Pacios, R. Inverted ITO-Free Organic Solar Cells Based on P and N Semiconducting Oxides. New Designs for Integration in Tandem Cells, Top or Bottom Detecting Devices, and Photovoltaic Windows. *Energy Environ. Sci.* **2011**, *4*, 453−458.
(23) Dou, L.; Liu, Y.; Hong, Z.; Li, G.; Yang, Y. Low-Bandgap Near-IR Conjugated Polymers/Molecules for Organic Electronics. *Chem. Rev.* **2015**, *115* (23), 12633−12665.
(24) Kirchartz, T.; Agostinelli, T.; Campoy-Quiles, M.; Gong, W.; Nelson, J. Understanding the Thickness-Dependent Performance of Organic Bulk Heterojunction Solar Cells: The Influence of Mobility, Lifetime, and Space Charge. *J. Phys. Chem. Lett.* **2012**, *3* (23), 3470−3475.
(25) Lenes, M.; Koster, L. J. A.; Mihailetchi, V. D.; Blom, P. W. M. Thickness Dependence of the Efficiency of Polymer:fullerene Bulk Heterojunction Solar Cells. *Appl. Phys. Lett.* **2006**, *88* (24), 243502.
(26) *SU1024LE-1.7 InGaAs Linear Photodiode Array*. http://www.sensorsinc.com/images/uploads/documents/1024LE.pdf. (accessed on [date]).
(27) Downs, C.; Vandervelde, T. E. Progress in Infrared Photodetectors since 2000. *Sensors* **2013**, *13* (4), 5054−5098.
(28) Noriega, R.; Rivnay, J.; Vandewal, K.; Koch, F. P. V; Stingelin, N.; Smith, P.; Toney, M. F.; Salleo, A. A General Relationship between Disorder, Aggregation and Charge Transport in Conjugated Polymers. *Nat. Mater.* **2013**, *12* (11), 1038−1044.
(29) Beiley, Z. M.; Hoke, E. T.; Noriega, R.; Dacuña, J.; Burkhard, G. F.; Bartelt, J. A.; Salleo, A.; Toney, M. F.; McGehee, M. D. Morphology-Dependent Trap Formation in High Performance Polymer Bulk Heterojunction Solar Cells. *Adv. Energy Mater.* **2011**, *1* (5), 954−962.
(30) Peumans, P.; Bulovic, V.; Forrest, S. R. Efficient, High-Bandwidth Organic Multilayer Photodetectors. *Appl. Phys. Lett.* **2000**, *76* (2000), 3855−3857.
(31) Xue, J.; Forrest, S. R. Carrier Transport in Multilayer Organic Photodetectors: I. Effects of Layer Structure on Dark Current and Photoresponse. *J. Appl. Phys.* **2004**, *95* (4), 1859−1868.

DOI: 10.1021/acsami.6b12162
ACS Appl. Mater. Interfaces XXXX, XXX, XXX−XXX

(32) Servaites, J. D.; Ratner, M. A.; Marks, T. J. Organic Solar Cells: A New Look at Traditional Models. *Energy Environ. Sci.* **2011**, *4* (11), 4410−4422.
(33) Clarke, T. M.; Durrant, J. R. Charge Photogeneration in Organic Solar Cells. *Chem. Rev.* **2010**, *110* (11), 6736−6767.
(34) Street, R. A.; Krakaris, A.; Cowan, S. R. Recombination through Different Types of Localized States in Organic Solar Cells. *Adv. Funct. Mater.* **2012**, *22* (21), 4608−4619.
(35) Guan, Z.; Li, H.-W.; Cheng, Y.; Yang, Q. D.; Lo, M.-F.; Ng, T.-W.; Tsang, S.-W.; Lee, C.-S. The Charge-Transfer State Energy and Its Relationship with Open-Circuit Voltage in Organic Photovoltaic Device. *J. Phys. Chem. C* **2016**, *120* (26), 14059−14068.
(36) Prokes, A. Influence of Temperature Variation on Optical Receiver Sensitivity and Its Compensation. *Radioengineering* **2007**, *16* (3), 13−18.
(37) Lochner, C. M.; Khan, Y.; Pierre, A.; Arias, A. C. All-Organic Optoelectronic Sensor for Pulse Oximetry. *Nat. Commun.* **2014**, *5*, 5745.
(38) Yokota, T.; Zalar, P.; Kaltenbrunner, M.; Jinno, H.; Matsuhisa, N.; Kitanosako, H.; Tachibana, Y.; Yukita, W.; Koizumi, M.; Someya, T. Ultraflexible Organic Photonic Skin. *Sci. Adv.* **2016**, *2* (4), e1501856−e1501856.

DOI: 10.1021/acsami.6b12162
ACS Appl. Mater. Interfaces XXXX, XXX, XXX−XXX